

Modelling synchrotron and synchrotron self-Compton emission of gamma-ray burst afterglows from radio to very-high energies

Jagdish C. Joshi^{1,2,3} * and Soebur Razzaque¹ †

¹Centre for Astro-Particle Physics (CAPP) and Department of Physics, University of Johannesburg, PO Box 524, Auckland Park 2006, South Africa

²School of Astronomy and Space Science, Nanjing University, Nanjing 210093, China

³Key laboratory of Modern Astronomy and Astrophysics (Nanjing University), Ministry of Education, Nanjing 210093, China

10 May 2021

ABSTRACT

Synchrotron radiation from a decelerating blastwave is a widely accepted model of radio to X-ray afterglow emission from gamma-ray bursts (GRBs). GeV gamma-ray emission detected by the Fermi Large Area Telescope (LAT) and the duration of which extends beyond the prompt gamma-ray emission phase, is also compatible with broad features of afterglow emission. We revisit the synchrotron self-Compton (SSC) emission model from a decelerating blastwave to fit multiwavelength data from three bright GRBs, namely GRB 190114C, GRB 130427A and GRB 090510. We constrain the afterglow model parameters using the simultaneous fit of the spectral energy distributions at different times and light curves at different frequencies for these bursts. We find that a constant density interstellar medium is favored for the short GRB 090510, while a wind-type environment is favored for the long GRB 130427A and GRB 190114C. The sub-TeV component in GRB 190114C detected by MAGIC is the SSC emission in our modelling. Furthermore we find that the SSC emission in the Thomson regime is adequate to fit the spectra and light curves of GRB 190114C. For the other two GRBs, lacking sub-TeV detection, the SSC emissions are also modeled in the Thomson regime. For the model parameters we have used, the $\gamma\gamma$ attenuation in the blastwave is negligible in the sub-TeV range compared to the redshift-dependent $\gamma\gamma$ attenuation in the extragalactic background light.

Key words: Gamma-Ray Bursts : GeV-TeV Component, Multiwavelength Emission

1 INTRODUCTION

Afterglow emission occurs in GRBs after the trigger of a burst which produces the prompt emission. The afterglows are important to understand the radiative processes and the source environments in GRBs, located at cosmological distances. The afterglow emission from GRBs were predicted in radio, optical/UV, X-rays and GeV-TeV bands (Paczynski & Rhoads 1993; Meszaros et al. 1994; Mészáros & Rees 1997; Vietri 1997; Panaitescu & Mészáros 1999; Sari et al. 1998; Chiang & Dermer 1999; Chevalier & Li 2000; Zhang & Mészáros 2001; Sari & Esin 2001; Granot & Sari 2002; Berger 2014; Kumar & Zhang 2015). The discovery of X-ray and optical afterglow emission from GRB 970228 gave the first hint for the success of GRB afterglow models (Costa et al. 1997; van Paradijs et al. 1997). Most of the afterglow radiation features are usually explained using the synchrotron model by Sari et al. (1998). More recently the synchrotron models have been successful to interpret Fermi-LAT observations of

late GeV emission from GRBs (Kumar & Barniol Duran 2009; Ghisellini et al. 2010; Razzaque et al. 2010; Pandey et al. 2010); see also Gehrels & Razzaque (2013) for reviews of GeV emission. The recent detection of a sub-TeV spectral component from GRB 190114C and GRB 190829A compliments the expectation of the GRB afterglow models (MAGIC Collaboration et al. 2019a; Abdalla et al. 2019; de Naurois 2019; MAGIC Collaboration et al. 2019b; Zhang 2019).

Physical processes in addition to the synchrotron radiation are required once the photons detected from the afterglow reached above the maximum synchrotron energy limit. The most efficient process to produce GeV-TeV emission is upscattering of synchrotron photons by the same electrons, known as the synchrotron self-Compton (SSC) or inverse-Compton emission. The intensity of the self-Compton signals from the blastwaves, when they interact with the circumburst medium, was predicted by Meszaros & Rees (1994). More detailed calculations were carried out later on by Chiang & Dermer (1999), Panaitescu & Kumar (2000), Zhang & Mészáros (2001), and by Sari & Esin (2001). For the detectability of the SSC component in the afterglow, a higher density; greater than 1 cm^{-3} ; has been estimated by Sari & Esin

* jjoshi@nuj.edu.cn

† srazzaque@uj.ac.za

(2001). The search for this component in GRBs was performed using the Fermi-LAT data and the SSC process was used to explain the delayed GeV component in GRB afterglows (Liu et al. 2013; Panaitescu et al. 2013; Wang et al. 2019). More recently, High Energy Stereoscopic System (HESS) detected sub-TeV emission from GRB 180720B and GRB 190829A with high significance (Abdalla et al. 2019; de Naurois 2019). These detections have renewed modelling activities of these bursts (see, e.g., Fraija et al. 2019a,b,c; Derishev & Piran 2019; Zhang et al. 2019; Ronchi et al. 2020; Chand et al. 2020).

In this work we revisit the SSC model by Sari & Esin (2001) and show its application to the two GeV bright bursts, namely GRB 090510 and GRB 130427A, and to the MAGIC-detected burst GRB 190114C. The model has been presented for the afterglow emission from the forward shock of an adiabatic blastwave decelerating in a constant density or wind-type environment. We constrain the afterglow model parameters using simultaneous fits to the radio to gamma-ray light curves and spectra at different times after the prompt emission.

The outline of this paper is the following. In Section 2, we discuss the dynamics of the blastwave. In Section 3 we discuss the synchrotron emission model and continue with SSC model in Section 4. In Section 5 we discuss absorption of sub-TeV photons in the blastwave and apply our model to GRBs in section 6. We discuss our results in Section 7 and conclude our work in Section 8. The derivation of synchrotron self-absorption frequency and numerical values of the model parameters for different blastwave evolution scenarios used in modeling are given in the Appendices.

2 BLASTWAVE MODELLING

The GRB event triggers a blastwave, with injected kinetic energy E_k , into the surrounding medium which slows down with time (Blandford & McKee 1976). For a generic density profile $\propto AR^{-s}$ of the surrounding medium at a distance R from the explosion center, the blastwave energy is given by $E_k = 8\pi AR^{3-s}\Gamma^2 c^2 / (17 - 4s)$, where Γ is the Lorentz factor of the shock front (Blandford & McKee 1976; Chevalier & Li 2000). We calculate the deceleration time of the blastwave by equating the blastwave energy to E_k and using time $t = (1+z)R/2\Gamma^2 c$ as measured by an observer (Rees & Meszaros 1992) as

$$t_{\text{dec},i} = \left[\frac{17E_k(1+z)^3}{64\pi n m_p c^5 \Gamma^8} \right]^{1/3} = 59.6(1+z)n_0^{-1/3}\Gamma_{2.5}^{-8/3}E_{55}^{1/3} \text{ s.} \quad (1)$$

for the case ($s = 0$) of interstellar medium of constant gas density n per cubic centimeter. For numerical values, we have used $n = n_0 \text{ cm}^{-3}$, $E_k = 10^{55} E_{55} \text{ erg}$ and $\Gamma = 10^{2.5} \Gamma_{2.5}$ (with notation $X = 10^n X_n$). For the case ($s = 2$) of wind environment typically used for GRB afterglow modeling,

$$t_{\text{dec},w} = \frac{9E_k(1+z)}{16\pi A m_p c^3 \Gamma^4} = 13.3(1+z)A_*^{-1}\Gamma_{2.5}^{-4}E_{55} \text{ s.} \quad (2)$$

For numerical values, we have considered the mass-loss rate by the progenitor star is $\dot{M}_w = 10^{-5} \dot{M}_{-5} M_\odot \text{ yr}^{-1}$, having a wind velocity $v_w = 10^8 v_8 \text{ cm s}^{-1}$. Therefore $A = \dot{M}/(4\pi v_w m_p) = 3.02 \times 10^{35} A_* \text{ cm}^{-1}$, where $A_* \equiv \dot{M}_{-5}/v_8$.

For an observer viewing the blastwave along the line of sight to the center, the expansion takes place with the Lorentz factor of the shocked fluid or gas $\Gamma_g = \Gamma/\sqrt{2}$, for a strong shock. The blastwave radius evolution with time after the onset of deceleration is

given by

$$R_i(t) = \frac{16\Gamma_{g,i}^2(t)ct}{1+z} \quad (3)$$

and

$$R_w(t) = \frac{8\Gamma_{g,w}^2(t)ct}{1+z}, \quad (4)$$

respectively for the ISM (Sari 1997) and wind (Panaitescu & Mészáros 1998; Dai & Lu 1998) environments. Subsequently after the deceleration time, the Lorentz factor of the shocked fluid evolves with time as

$$\Gamma_{g,i}(t) = \frac{\Gamma}{2^{3/4}} \left(\frac{t_{\text{dec},i}}{t} \right)^{3/8} \quad (5)$$

and

$$\Gamma_{g,w}(t) = \frac{\Gamma}{2^{3/4}} \left(\frac{t_{\text{dec},w}}{t} \right)^{1/4} \quad (6)$$

respectively for the ISM and wind.

3 SYNCHROTRON EMISSION

The electrons accelerated at the external shock region radiate away their energy in the amplified magnetic field (see, e.g., Piran 1999; Zhang & Mészáros 2004b). The magnetic field takes away a fraction ϵ_B of the total shock energy, and can be expressed as (all jet-frame quantities are denoted with primes)

$$\begin{aligned} B'_i(t) &= [32\pi\epsilon_B n_0 m_p c^2]^{1/2} \Gamma_g(t) \\ B'_w(t) &= [32\pi\epsilon_B A R^{-2} m_p c^2]^{1/2} \Gamma_g(t) \end{aligned} \quad (7)$$

for the ISM and wind cases, respectively. For convenience, we report numerical values of the model parameters for an adiabatic blastwave expansion in these two different scenarios in the Appendix. We discuss shock-accelerated electron spectrum and characteristic breaks therein next.

3.1 Characteristic electron Lorentz factors

We consider that the accelerated electrons follow a power-law spectrum which is defined as $N_e(\gamma'_e) = K\gamma_e'^{-p}$, with spectral index p and normalization $K = (p-1)n'\gamma_m'^{p-1}$. The power-law electron energy distribution to model the GRB afterglows can have a broad spectral index in the range of 1.4-2.8 as found in a set of GRBs by Panaitescu & Kumar (2001). The characteristic Lorentz factor of the accelerated electrons at the forward shock for $p > 2$ is given by (Sari et al. 1998),

$$\gamma'_m(t) = \left[\frac{m_p}{m_e} \epsilon_e \frac{p-2}{p-1} \Gamma_g \right]; p > 2 \quad (8)$$

The radiation by electrons in the spectrum has two phases of emission called the fast- and slow-cooling. In the fast-cooling, most of the electrons produce the emission efficiently within the dynamic time, while in the slow-cooling, only the high-energy part of the spectrum, above a cooling Lorentz factor γ'_c , cools efficiently. The electron spectrum defined above will be modified in the fast-cooling regime as

$$N_e(\gamma'_e) \propto \begin{cases} \gamma_e'^{-2}, & \gamma'_c \leq \gamma'_e \leq \gamma'_m \\ \gamma_e'^{-p-1}, & \gamma'_e > \gamma'_m, \end{cases} \quad (9)$$

and in the slow-cooling regime as

$$N_e(\gamma'_e) \propto \begin{cases} \gamma'^{-p}; & \gamma'_m \leq \gamma'_e \leq \gamma'_c \\ \gamma'^{-p-1}, & \gamma'_e > \gamma'_c. \end{cases} \quad (10)$$

The cooling Lorentz factor (γ'_c), can be estimated by comparing the total cooling time $t'_c = 6\pi m_e c / [\sigma_T B'^2 \gamma'_c (1 + Y)]$ with the dynamic or expansion time scale $t'_{dyn} = t\Gamma_g / (1 + z)$ as

$$\gamma'_c(t) = \left[\frac{6\pi m_e c^2 (1 + z)}{\sigma_T c B'^2(t) t \Gamma_g (1 + Y)} \right]. \quad (11)$$

Here, σ_T is the Thomson cross-section and $Y \equiv L_{ssc} / L_{sy}$ is the Comptonization parameter, which is the ratio between the SSC and synchrotron luminosities. In the case of fast-cooling the Y -parameter can be simply expressed as (Sari & Esin 2001)

$$Y(\text{fast}) = \begin{cases} \epsilon_e / \epsilon_B; & \epsilon_e / \epsilon_B \ll 1 \\ \sqrt{\epsilon_e / \epsilon_B}; & \epsilon_e / \epsilon_B \gg 1 \end{cases} \quad (12)$$

We investigate the SSC component in GRBs where slow cooling is needed and we explore $Y \gg 1$ scenario for which we define the expression of Y based on Sari & Esin (2001)

$$Y(\text{slow}) = \sqrt{\epsilon_e / \epsilon_B} \times \begin{cases} (t/t_0^{\text{SSC}})^{(2-p)/[2(4-p)]}; & \text{Adiabatic - ISM} \\ (t/t_0^{\text{SSC}})^{(2-p)/(4-p)}; & \text{Adiabatic - Wind} \end{cases} \quad (13)$$

The transition time t_0 from the fast- to slow-cooling spectra is defined as $\nu_m(t_0) = \nu_c(t_0)$, and in the presence of SSC cooling of electrons one needs to use the SSC transition time t_0^{SSC} or t_0^{IC} (Sari & Esin 2001). The maximum photon energy emitted by synchrotron cooling is proportional to the saturation Lorentz factor (γ'_s). This is calculated by equating the accelerating time scale $t'_{acc} = \phi \gamma'_e m_e c / [eB'(t)]$, where ϕ^{-1} is the acceleration efficiency for electrons, with the total cooling time t'_c defined earlier as,

$$\gamma'_s(t) = \left[\frac{6\pi e}{\phi \sigma_T B'(t) (1 + Y)} \right]. \quad (14)$$

Typically $\phi = 10$ is assumed and $\phi = 1$ correspond to the maximum efficiency. Again, we report numerical values and parameter dependence of the characteristic Lorentz factors for different fireball evolution scenarios in the Appendix.

3.2 Synchrotron spectra and break frequencies

The synchrotron break frequencies for the electron Lorentz factors γ'_e are related by the expression (Razzaque 2013),

$$h\nu(t) = \frac{3}{2} \frac{B'(t)}{B_Q} m_e c^2 \frac{\Gamma_g(t)}{1 + z} \gamma'^2 \quad (15)$$

where $B_Q = 4.41 \times 10^{13}$ G. Using equation (15) we can calculate the synchrotron break frequencies for the minimum (ν'_m), cooling (ν'_c) and saturation (ν'_s) Lorentz factors γ'_m , γ'_c and γ'_s , respectively. These frequencies in the jet frame are transformed to the observer frame by the relations $\nu = \nu' \Gamma / (1 + z)$. The synchrotron radiation spectrum from these electrons is distributed in particular frequency order, depending on the fast- and slow-cooling (Sari et al. 1998; Granot & Sari 2002; Thomas et al. 2017). The flux of synchrotron radiation is given in the fast-cooling case as

$$F_{\nu, \text{fast}} = f_{\nu, \text{max}} \begin{cases} \left(\frac{\nu}{\nu_a}\right)^2 \left(\frac{\nu_a}{\nu_c}\right)^{1/3}; & \nu < \nu_a \\ \left(\frac{\nu}{\nu_c}\right)^{1/3}; & \nu_a \leq \nu \leq \nu_c \\ \left(\frac{\nu}{\nu_c}\right)^{-1/2}; & \nu_c < \nu < \nu_m \\ \left(\frac{\nu_m}{\nu_c}\right)^{-1/2} \left(\frac{\nu}{\nu_m}\right)^{-p/2}; & \nu \geq \nu_m, \end{cases} \quad (16)$$

and in the slow-cooling as

$$F_{\nu, \text{slow}} = f_{\nu, \text{max}} \begin{cases} \left(\frac{\nu}{\nu_a}\right)^2 \left(\frac{\nu_a}{\nu_m}\right)^{1/3}; & \nu < \nu_a \\ \left(\frac{\nu}{\nu_m}\right)^{1/3}; & \nu_a \leq \nu \leq \nu_m \\ \left(\frac{\nu}{\nu_m}\right)^{-(p-1)/2}; & \nu_m < \nu < \nu_c \\ \left(\frac{\nu}{\nu_m}\right)^{-(p-1)/2} \left(\frac{\nu}{\nu_c}\right)^{-p/2}; & \nu \geq \nu_c. \end{cases} \quad (17)$$

Here $f_{\nu, \text{max}}$ is the maximum synchrotron flux density which is defined as (Sari et al. 1998; Razzaque 2013),

$$f_{\nu, \text{max}} = \frac{N}{4\pi d_L^2} \frac{P(\gamma'_m)}{\nu_m} \frac{\Gamma_g^2}{(1 + z)^2}, \quad (18)$$

with the synchrotron power at γ'_m is given by $P(\gamma'_m) = c\sigma_T B'^2 \gamma'^2 / 6\pi$ (Rybicki & Lightman 1986). The total number of electrons in the blastwave is given by $N = (4/3)\pi R^3 n$, and the luminosity distance to the source is given by d_L . The time-dependence of the synchrotron flux is governed by the time-dependence of $f_{\nu, \text{max}}$ and of various break frequencies. Depending on a particular frequency band being observed, the break frequencies can pass through that band at different times. Two particularly interesting frequencies are ν_m and ν_c , and the time they appear in the spectrum t_m and t_c , respectively, are reported in the Appendix for the two different blastwave evolution scenarios. The time and frequency evolution of the flux, denoted as $F_\nu \propto t^\alpha \nu^\beta$, give rise to particular relations between α and β for different segments in equations (16) and (17). We report these so-called closure relations (Sari et al. 1998; Granot & Sari 2002; Zhang & Mészáros 2004a) for the synchrotron flux in Table 2. The maximum flux $f_{\nu, \text{max}}$, synchrotron self-absorption frequency ν_a and various other break frequencies are reported in the Appendix.

4 SYNCHROTRON SELF-COMPTON EMISSION

The SSC spectrum for the same electrons up-scattering synchrotron photons in the Thomson regime is analytically approximated by power-law segments with break frequencies given, following Sari & Esin (2001), by

$$\begin{aligned} \nu_a^{\text{SSC}} &\approx 2\gamma_m^2 \nu_a \\ \nu_m^{\text{SSC}} &\approx 2\gamma_m^2 \nu_m \\ \nu_c^{\text{SSC}} &\approx 2\gamma_c^2 \nu_c \end{aligned} \quad (19)$$

For this component of the spectrum we follow a similar flux distribution as for the synchrotron part with a shift in frequency as defined above. Similar to the maximum synchrotron flux $f_{\nu, \text{max}}$ in equation (18), we define the maximum SSC flux, which is based on the formalism discussed in Zhang & Mészáros (2001), as

$$f_{\nu, \text{max}}^{\text{SSC}} = \frac{\nu_m^{\text{sy}} U'_{\text{ph}}}{\nu_m^{\text{SSC}} U'_B} f_{\nu, \text{max}}. \quad (20)$$

Here the magnetic energy density is $U'_B = B'^2 / 8\pi$ and the photon energy density is $U'_{\text{ph}} = (16/3)\sigma_T U'_B \gamma_m^2 R(t)n(R)$.

We also calculate the SSC spectra using the smooth approximation discussed by Sari & Esin (2001), where the target synchrotron photon spectrum is integrated. For details of this approximation we refer to the Appendix A of their paper.

The fast- and slow-cooling SSC spectra in the Thomson regime follow the same ordering as for the synchrotron spectra. From the flux distribution we can calculate its dependence on the

frequency and time, $F_\nu \propto t^\alpha \nu^\beta$, for SSC emission in the two scenarios of blastwave expansions (Panaitescu & Kumar 2000). The temporal and frequency dependence of the fluxes are given in Table 2. The Klein-Nishina effect, however, can become important for SSC emission at very-high energies, which we discuss next.

4.1 Maximum Energy of Photons in Thomson Scattering Regime

Klein-Nishina effect in the IC scattering is important for electrons with Lorentz factor above $\gamma' \approx m_e c^2 / h\nu'$, for scattering photons of frequency ν' in the jet frame. This corresponds to a maximum or cutoff SSC photon energy in the Thomson regime as

$$E_{\gamma, \text{cut}}^{\text{SSC}} \approx \frac{m_e^2 c^4}{h\nu} \frac{\Gamma_g^2}{(1+z)^2}. \quad (21)$$

Photons above this energy are produced inefficiently in the Klein-Nishina regime, where $\nu^{\text{SSC}} \approx \gamma' \nu$, and the SSC flux decreases. Slow cooling case is described here for which the peak synchrotron flux is at ν_c . The corresponding cutoff photon energy via Thomson scattering is

$$E_{\gamma, \text{cut}}^{\text{SSC}} = 1.1 (1+z)^{-3/4} n_{0,-5}^{3/4} E_{55}^{3/4} \epsilon_{B,-1}^{3/2} t_2^{-1/4} (1+Y)^2 \text{ TeV} \quad (22)$$

for a constant-density environment with density $n_0 = 10^{-5} n_{0,-5} \text{ cm}^{-3}$ and

$$E_{\gamma, \text{cut}}^{\text{SSC}} = 5.5 A_{*, -2}^{3/2} \epsilon_{B,-1}^{3/2} t_2^{-1} (1+Y)^2 \text{ TeV} \quad (23)$$

for the wind environment with the wind parameter $A_* = 10^{-2} A_{*, -2}$. Therefore, the Klein-Nishina effect becomes important in the TeV energy range. We explicitly calculate this energy for GRB 190114C later on, indicating that the sub-TeV MAGIC detection can be modeled as SSC emission in the Thomson regime.

Note that these cutoff energies are larger than the photon energies, few hundred GeV, at which absorption due to $\gamma\gamma \rightarrow e^\pm$ interactions with the extragalactic background light (EBL) becomes important for cosmological distances (Razzaque et al. 2009; Finke et al. 2010). Therefore, direct detection of a Klein-Nishina effect in the TeV energy range of the GRB spectra can be difficult.

5 INTERNAL ABSORPTION IN THE BLASTWAVE

In this section we discuss absorption of gamma-rays within the forward shock due to $\gamma\gamma \rightarrow e^\pm$ interactions with synchrotron photons. The comoving number density of the synchrotron photons with frequency ν can be calculated from the corresponding observed flux F_ν as

$$n'_\nu = \left(\frac{d_L}{R} \right)^2 \frac{1+z}{\Gamma h c} F_\nu \quad (24)$$

As such, the $\gamma\gamma$ optical depth corresponding to that frequency can be calculated in delta-function approximation as

$$\tau_{\gamma\gamma} = \left(\frac{\sigma_T}{5} \right) \frac{n'_\nu R}{\Gamma_g} \quad (25)$$

This affects the photons of energy

$$E_\gamma = \frac{2m_e^2 c^4 \Gamma_g^2}{(1+z)^2 h\nu} \quad (26)$$

For an estimate, we use $F_\nu = f_{\nu, \text{max}}$ at $h\nu_c$ for the slow-cooling spectra to approximate the maximum optical depth for gamma-rays. These give the opacities in the ISM and wind environments

as

$$\tau_{\gamma\gamma, \text{ISM}} = 0.08 (1+z)^{-1/2} n_{0,-5} \epsilon_{B,-1}^{1/2} E_{55}^{-1/2} t_2^{1/2} \quad (27)$$

$$\tau_{\gamma\gamma, \text{wind}} = 0.4 (1+z)^{1/2} A_{*, -2}^2 \epsilon_{B,-1}^{1/2} E_{55}^{-1/2} t_2^{-1/2} \quad (28)$$

respectively. The corresponding gamma-ray energies are $E_\gamma \approx 2E_{\gamma, \text{cut}}^{\text{SSC}}$, where $E_{\gamma, \text{cut}}^{\text{SSC}}$ is found from equations (22) and (23), respectively, for the ISM and wind.

We have also calculated the $\gamma\gamma$ optical depth, for the full target photon distribution using (Gould & Schröder 1967)

$$\tau_{\gamma\gamma}(E_\gamma) = \frac{R}{\Gamma_g} \pi r_0^2 \left[\frac{m_e c^4 \Gamma_g}{(1+z) E_\gamma} \right]^2 \times \int_{\frac{m_e c^4 \Gamma_g}{(1+z) E_\gamma}}^{(1+z) E_\gamma / \Gamma_g} \frac{n'(\epsilon')}{\epsilon'^2} \phi[S_0(\epsilon')] d\epsilon', \quad (29)$$

where $\epsilon' = h\nu'$ and $n'(\epsilon') d\epsilon' = n'_\nu$. The function $\phi[S_0(\epsilon')]$ is given in Brown et al. (1973) and the argument is defined as $S_0(\epsilon') = (1+z)\epsilon' E_\gamma / \Gamma_g m_e^2 c^4$. This calculation assumes that the target photons are distributed isotropically in the blastwave.

Our results from numerical calculations are shown in Figure 1 where we consider the target photon distribution at times $t = 100\text{s}$ for GRB 090510, $t = 352 - 403\text{s}$ for GRB 130427A and $t = 68 - 110\text{s}$ for GRB 190114C. These values are similar to our analytical calculation of the optical depths, which serve as cross checks. As shown, the internal $\gamma\gamma$ opacity is negligible below the TeV energy range for the set of parameters we have used in this work. As such we do not consider secondary cascade emission. We have also plotted in Figure 1 the $\gamma\gamma$ opacity due to EBL using Finke et al. (2010) model. EBL attenuation is significant for $\gtrsim 100$ GeV range and determines the maximum observable photon energy from GRBs studied here.

6 MODELLING OF BROAD-BAND AFTERGLOW EMISSION

We investigate the afterglow emission of GeV-bright bursts, namely the short GRB 090510, long GRB 130427A, as well as the recently-detected long GRB 190114C. We describe the details of their emission in next subsections. The parameters used in modelling the afterglow emission of these GRBs, are given in Table 1. We also show the CTA sensitivity in the SEDs and light curves. In the light curves the sensitivity is plotted at 25 GeV and at 250 GeV. In the SEDs, the CTA sensitivity is shown for a duration of 300-1000 s. In such calculations, a 5σ significance is required in each energy bin and the source flux needs to be few times higher than the background signal. These sensitivities for 25 events in each bin, where 4 bins are taken per decade of energy, is calculated by Funk et al. (2013). These calculations show that the differential flux sensitivity of CTA for 25 GeV gamma-rays is approximately $10^{-9} \text{ erg cm}^{-2} \text{ s}^{-1}$ if the transient source lifetime is considered to be within 10 s. In our work we have used the CTA sensitivity for transients calculated at an elevation angle 70° , which has been retrieved from the CTA website¹.

6.1 Short GRB 090510

The GRB 090510 with a duration of $T_{90} = 0.3 \pm 0.07 \text{ s}$ was observed in the early afterglow phase by the Swift and Fermi

¹ <https://www.cta-observatory.org/science/cta-performance/>

Table 1. The afterglow model parameters from simultaneous interpretation of the SED and light curves.

Parameter	GRB 090510	GRB 130427A	GRB 190114C
E_k (erg)	9×10^{51}	3×10^{54}	4×10^{54}
Γ	1500	280	300
t_{dec} (s)	4.5	98.1	52.6
t_0^{SSC} (s)	0.0001	25.5	8.6
t_{jet} (s)	3000	-	-
A_* (cm $^{-1}$)	-	1×10^{-2}	2×10^{-2} (6×10^{-2})
n_0 (cm $^{-3}$)	1×10^{-5}	-	-
p	2.3	2.05	2.18 (2.1)
ϵ_e	0.2	0.27	0.033 (0.034)
ϵ_B	0.02	0.015	0.012 (0.0039)
Y (slow)	$0.93t_2^{-0.09}$	$4.1t_2^{-0.03}$	$1.3t_2^{-0.1}$
ϕ	10	1	1

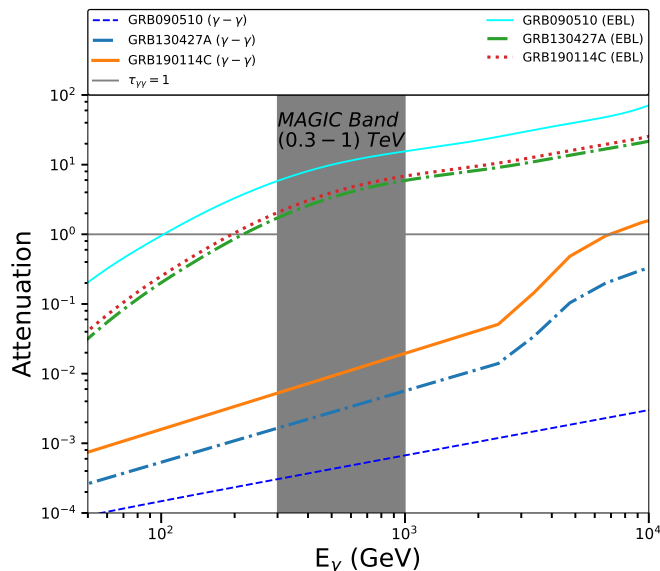


Figure 1. The $\gamma\gamma \rightarrow e^\pm$ optical depths in the blastwave and in the EBL. The blastwave opacities are calculated for the observed GeV-TeV radiation in the target photon field. These values are estimated at 68 s for GRB 190114C, at 352 s for GRB 130427A, and at 100 s for GRB 090510 where the density of target photons is the maximum for each case. The EBL optical depths for the model by Finke et al. (2010).

satellites (De Pasquale et al. 2010). The redshift of the burst is $z = 0.903 \pm 0.003$ (Rau et al. 2009) and the corresponding luminosity distance is 1.8×10^{28} cm. These observations were modeled using typical synchrotron radiation (De Pasquale et al. 2010; Ghirlanda et al. 2010; He et al. 2011; Fraija et al. 2016b). A combined electron-proton synchrotron model was used by Razzaque (2010), where the proton component was used to interpret the Fermi-LAT data. A two-component jet model was used by Corsi et al. (2010) to interpret the same data.

Figure 2 shows the data and our model curves for GRB 090510. Our interpretation favours a constant circumburst environment with a very low density of 1×10^{-5} cm $^{-3}$. The modelling of this source requires slow cooling of the relativistic electrons. The parameters are shown in Table 1 and fast to slow cooling transition occurs at $t_0^{\text{IC}} = 0.0001$ s. The no jet break model has surplus of flux in late times, which is corrected using the jet-break feature in this

source. In the jet-break, the time dependence of the break frequencies are $\nu_a \propto t^{-1/5}$, $\nu_m \propto t^{-2}$, and $\nu_c \propto t^0$ and the maximum flux goes as $f_{\nu, \text{max}} \propto t^{-1}$. During the jet-break phase the closure relations for slow cooling are $F_\nu \propto \nu^2 t^1$ for $\nu < \nu_a$ and $F_\nu \propto \nu^{1/3} t^{2/3}$ for the regime $\nu_a < \nu < \nu_m$. The late time emission needs a steeper dependence on time and the emission is explained using the regimes $\nu_m < \nu < \nu_c$ where $F_\nu \propto \nu^{-(p-1)/2} t^{1-p}$ and $\nu > \nu_c$ where $F_\nu \propto \nu^{-p/2} t^{1-p}$. The jet-break time is estimated using $t_{\text{jet}} = 5 \times 10^5 (1+z) (E_{55}/n)^{1/3} \theta_{-1}^{8/3}$ s (Sari et al. 1999). We find that the jet-break time is 3000 s, which is in the range of 1.4-5.1 ks, as discussed in Razzaque (2010).

Our modelling confirms the need for very low density ISM medium, as also shown in earlier results by Corsi et al. (2010). The maximum photon energy due to synchrotron emission with our model parameters is 1.8 GeV at 100 s (see the SEDs plotted in Fig. 2). The model for early two epochs i.e. 100 s and 150 s produces slightly higher amount of optical flux. In the LAT energy range and the remaining part of emission is well produced. For the redshift of GRB 090510 the EBL attenuation energy is ~ 100 GeV based on the EBL model by Finke et al. (2010) for which we have also plotted the $\gamma\gamma$ opacity in Fig. 1. The suppression of the SSC component plotted in Fig. 2 using smooth approximation is due to the EBL attenuation and $\gamma\gamma$ effects are negligible in the blastwave, based on our input model parameters.

The breaks in the light curves for 1 eV occurs at $t_m \sim 2500$ s and for 1 keV at $t_m \sim 25$ s. We have also shown in the light curve, bottom panel of Figure 2 the rising part before the deceleration time. For slow cooling, which is valid for this case, the rising part is defined as $F_{\nu, s} \propto t^2$ for $\nu < \nu_{a, s}$, $F_{\nu, s} \propto t^3$ for $\nu_{a, s} < \nu < \nu_{m, s}$, $F_{\nu, s} \propto t^3$ for $\nu_{m, s} < \nu < \nu_{c, s}$ and $F_{\nu, s} \propto t^2$ for $\nu > \nu_{c, s}$ (Sari & Piran 1999; Gao et al. 2013). The SSC emission has the temporal dependence for pre-deceleration is $F_{\nu, \text{SSC}} \propto t^3$ for $\nu_{m, \text{SSC}} < \nu < \nu_{c, \text{SSC}}$ and $F_{\nu, \text{SSC}} \propto t$ for $\nu > \nu_{c, \text{SSC}}$. For optical, XRT and BAT energy range we have $F_\nu \propto t^3$ and for the 100 MeV synchrotron flux it is proportional to t^2 , while for SSC emission at 25 GeV, $F_{\nu, \text{SSC}} \propto t^3$.

6.2 Long GRB 130427A

One of the brightest long GRB 130427A with $T_{90} = 276 \pm 5$ s was located at redshift $z = 0.34$ (Levan et al. 2013). The afterglow of GRB 130427A was observed up to 220 ks in radio and optical wavelengths while the X-ray and gamma-ray observations by Swift-XRT and Fermi-LAT were active upto 1.8 ks (Maselli et al. 2014). A photon of energy 95 GeV was detected at $T_0 + 244$ s and a 32 GeV photon was detected in late time at $T_0 + 34.4$ ks (Ackermann et al. 2014). Its association with a type-Ic supernova (Melandri et al. 2014) provides us further evidence that long GRB 130427A is produced by the collapse of a massive star. The light curves for this source has been modelled for constant density medium (Panaitescu et al. 2013; Maselli et al. 2014; Fan et al. 2013; Liu et al. 2013; Tam et al. 2013) as well as for wind medium (Kouveliotou et al. 2013; Panaitescu et al. 2013; Fraija et al. 2016a). The reverse shock emission features are also used in some models for this burst (Laskar et al. 2013a; Fraija et al. 2016a; Vestrand et al. 2014; Laskar et al. 2013b; Vestrand et al. 2014).

The SED and light curves from our modelling for this burst is shown in Fig. 3. The maximum photon energy due to synchrotron emission with our model parameters is 7.5 GeV at 352 s. We used a wind environment to explain the multiwavelength observations.

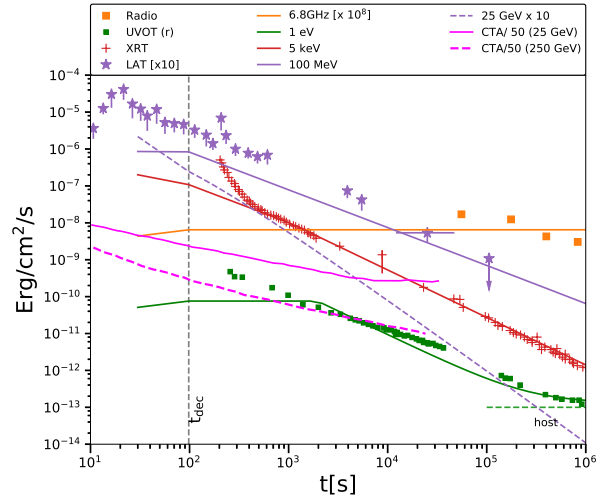
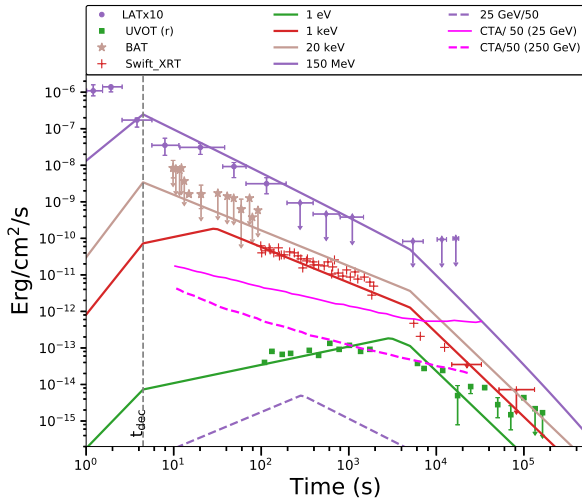
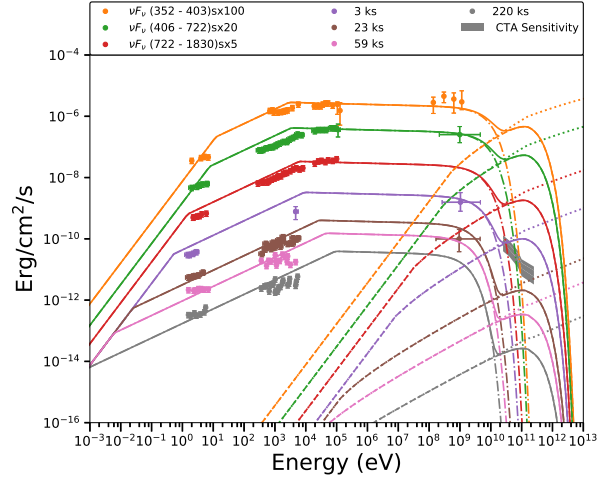
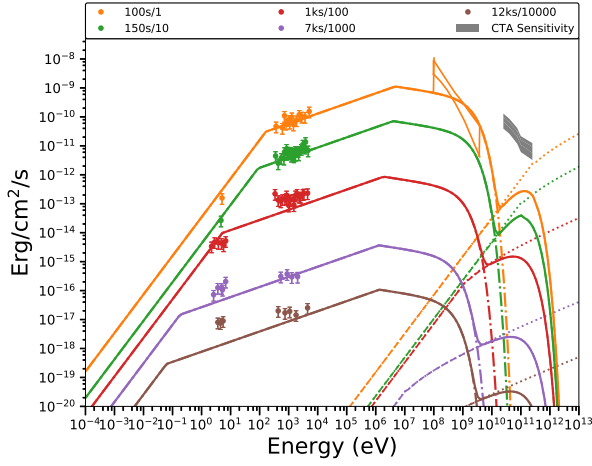


Figure 2. *Top Panel:* The SED of short GRB 090510, where the multiwavelength data are shown for the Swift and Fermi-LAT observations (De Pasquale et al. 2010). *Bottom Panel:* The Swift/BAT (15-350 keV), Swift/UVOT, and Swift/XRT (0.3-10keV), Fermi-LAT (100 MeV-4 GeV) light curves are shown. For the duration of 1.9-5.1 ks, there are no data points in Swift/XRT observation due to Earth occultation. The data points are taken from De Pasquale et al. (2010), SWIFT-XRT database <https://www.swift.ac.uk/analysis/xrt/>. The SED fluxes are scaled by factors 1, 10, 10^2 , 10^3 and 10^4 in decreasing order of time.

The parameters of our model are reported in Table 1. We estimate $E_{\gamma, \text{cut}}^{\text{SSC}}$ defined in equation (23) which is ~ 2.2 TeV at 352 s. The EBL attenuation for this redshift is ~ 300 GeV and we use Thomson scattering regime in our model. The early intervals of SED with duration 352-403 s, 403-722 s and 722-1830 s are modelled using times at 352 s, 722 s and 1830 s, respectively. The later SEDs are plotted with mentioned time in the figure legend. The internal $\gamma\gamma$ opacity is negligible (see Fig. 1). Therefore, we have used a cutoff energy of 300 GeV for the SED at all time in Fig. 3. The breaks in the light curves, for 2 eV is at $t_m \sim 1352$ s.

The pre-deceleration phase in our light curve, bottom panel of Figure 3 follows the dependence $F_{\nu, s} \propto t^2$ for $\nu < \nu_{a, s}$, $F_{\nu, s} \propto t^{1/3}$ for $\nu_{a, s} < \nu < \nu_{m, s}$, $F_{\nu, s} \propto t^{(1-p)/2}$ for $\nu_{m, s} < \nu < \nu_{c, s}$ and $F_{\nu, s} \propto t^{(2-p)/2}$ for $\nu > \nu_{c, s}$ (Sari & Piran 1999; Gao et al. 2013). The SSC emission has the temporal dependence for pre-deceleration is $F_{\nu, \text{SSC}} \propto t^{(1-p)/2}$ for $\nu_{m, \text{SSC}} < \nu < \nu_{c, \text{SSC}}$ and $F_{\nu, \text{SSC}} \propto t^{3/2}$ for $\nu > \nu_{c, \text{SSC}}$. For GRB 130427A before decel-

Figure 3. *Top Panel:* The SED of the long GRB 130427A, where in the optical the total contribution of the forward shock and host galaxy is shown. *Bottom Panel:* The light curves in optical to gamma-rays for GRB 130427A. The data used in these two plots: Radio 6.8 GHz, UVOT, (0.3-10) keV and LAT (0.1-100) GeV data are taken from Maselli et al. (2014) and from SWIFT-XRT database <https://www.swift.ac.uk/analysis/xrt/>.

eration time we have $t^{1/3}$ dependence for 6.8 GHz and 2 eV, and $t^{-0.52}$ for 5 keV and $t^{-0.02}$ for 100 MeV light curve. For the SSC light curve at 25 GeV the dependence is $t^{-0.52}$.

6.3 Long GRB 190114C

The sub-TeV GRB 190114C is located at a redshift $z = 0.4245 \pm 0.0005$ (Castro-Tirado et al. 2019). This is the first case of afterglow observation where a sub-TeV component was observed by the MAGIC ground-based Cherenkov telescope (MAGIC Collaboration et al. 2019a,b). The isotropic gamma-ray energy released in this burst was $(2.5 \pm 0.1) \times 10^{53}$ erg (MAGIC Collaboration et al. 2019b) and the burst duration is $T_{90} = 116.4 \pm 2.6$ s for 50-300 keV range (Ajello et al. 2020). The optical light curve in the early afterglow phase has a steeper index and shows the signatures of reverse shock emission (Laskar et al. 2019). It is widely believed that the observed sub-TeV component is the SSC emission from the blastwave.

We have modelled the SEDs and lightcurves of GRB 190114C

using an adiabatic blastwave in a wind environment. The SED and light curves from our modelling for this burst is shown in Fig. 4.

The SSC spectra are shown using analytical approximation (grey solid lines) and also using the smooth approximation (dotted orange curves). The MAGIC data in the SED with empty circles are the observed ones while the filled circles are the ones corrected for the EBL attenuation. In the light curves the MAGIC data are corrected for the EBL and the corresponding model output is plotted using smooth approximation for SSC emission. The sub-TeV components for the intervals 68-110 s and 110-180 s are modelled using times at 90 s and 150 s respectively. The two vertical lines correspond to the cutoff energy defined in equation (23) for these two intervals, i.e. $E_{\gamma,\text{cut}}^{\text{SSC}}(t = 90\text{s}) \sim 3.7$ TeV and $E_{\gamma,\text{cut}}^{\text{SSC}}(t = 150\text{s}) \sim 2.1$ TeV. This indicates that the Klein-Nishina effect for the SSC emission becomes important at energies above few 100 GeV, for some combination of afterglow model parameters. Hence, we can model the MAGIC detected photons from GRB 190114C in the Thomson scattering regime. It can also be seen from Fig. 1 that the internal $\gamma\gamma$ opacity is negligible and very high-energy photons are attenuated in the EBL. To model the SEDs we have used an EBL cutoff energy of 200 GeV at which the EBL opacity is ~ 1 for the model by Finke et al. (2010). In the light curve for this source in Fig. 4, only in optical bands the flux becomes harder for times $10^4 - 5 \times 10^5$ s and it cannot be explained using our one-zone model. The breaks in the light curves, for 97.5 GHz is at $t_m \sim 10^4$ s while for 18 GHz at $t_a = 732$ s and $t_m \sim 3 \times 10^4$ s. For GRB 190114C before deceleration time we have $t^{1/3}$ dependence for 18 and 97.5 GHz and 1 eV, and $t^{-0.6}$ for 5 keV and $t^{-0.1}$ for 100 MeV light curve. For the SSC light curve at 300 GeV the dependence is $t^{-0.6}$.

We have also obtained values for fit parameters (ϵ_e , ϵ_B , p and A_*), keeping other parameters same, for GRB 190114C using the analytic approximation of the SSC emission, in order to compare with the fit parameters obtained from the smooth approximation. The values of the fit parameters from analytic approximation are listed in Table 1 within parenthesis. We note that while the values of p and ϵ_e are comparable for both the approximations, the values of A_* is a factor of three larger and ϵ_B is a factor of three smaller for the analytic approximation. This has implications on the Y -parameter and subsequently on determining the Thomson or Klein-Nishina regime for SSC emission. In case of the analytic approximation, the Y -parameter will be larger than the more accurate smooth approximation.

7 DISCUSSION

In our modelling the blastwave is considered to be adiabatic and for GRB 090510 modelling we consider constant density ISM while for other two cases the medium is taken to be wind medium. This selection was inspired from the progenitor point of view for short and long GRBs, as most probably short GRBs bursts in a constant density medium while long GRBs takes place in the wind of progenitor star. The value of Γ is used to tune the value of deceleration time t_{dec} such that the emission hits the afterglow phase. The fast to slow cooling transition time t_0^{sc} in all three scenarios is such that the afterglow emission is explained using slow cooling.

We need $\Gamma = 1500$ to optimize the deceleration time for GRB 090510. In earlier works, value of $\Gamma = 2000$ is used by Ghirlanda et al. (2010) and combination of larger 10^4 and smaller value 220 is used by (Corsi et al. 2010) for narrow and wider jets. The low density medium used for GRB 090510 is also found in ear-

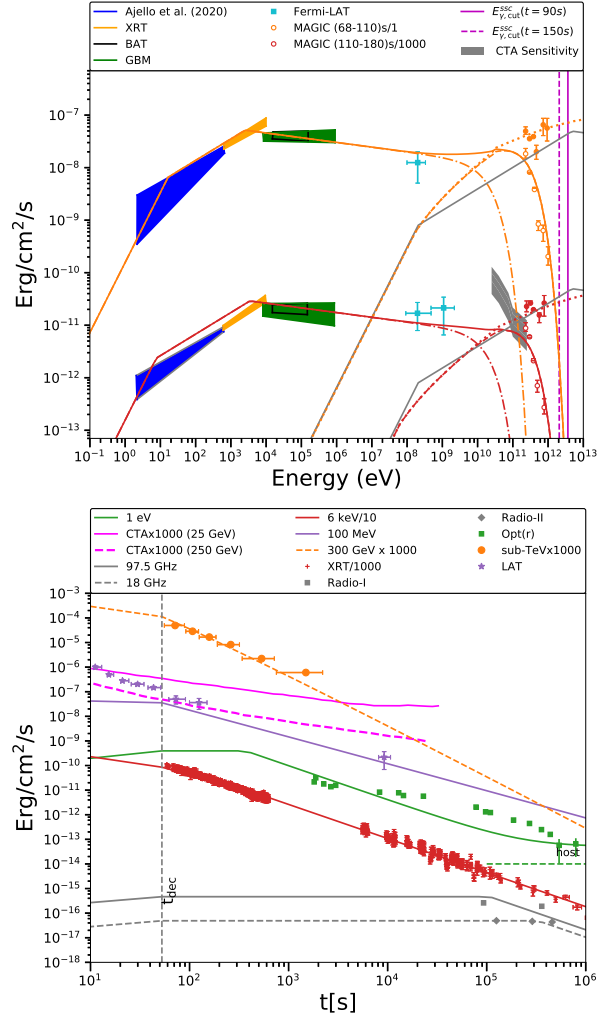


Figure 4. *Top Panel:* The SED of the long GRB 190114C and we have shown our model fit to MAGIC sub TeV data. *Bottom Panel:* The data used in these two plots: Radio 18 and 97.5 GHz, XRT (0.3-10) keV, BAT (15-150) keV, GBM (10 - 10^4) keV, LAT (0.1-100) GeV are taken from Ajello et al. (2020); MAGIC Collaboration et al. (2019b) and SWIFT-XRT database <https://www.swift.ac.uk/analysis/xrt/>. Note that the optical range data is actually a model based extrapolation as described by Ajello et al. (2020). The vertical solid and dashed magenta color lines shows the crossover from Thomson to Klein-Nishina regime.

lier work by (Corsi et al. 2010) but higher value 0.1 cm^{-3} is also reported (Fraija et al. 2016b). The jet-break feature is found at ~ 3 ks as indicated by the optical and X-ray light curves modelling and this is consistent with earlier work (Razzaque 2010).

For long GRB 130427A and GRB 190114C in the optical emission for time larger than 3×10^5 s, we have added the host galaxy emission to the SEDs. In GRB 190114C the reason for the harder optical emission in between $10^4 - 10^5$ s could be refreshed shock (Rees & Mészáros 1998; Granot et al. 2003). We found 10 times stronger wind in our model for GRB 130427A, $\dot{M}_{-5}/v_8 = 0.01$ compared to Panaitescu et al. (2013), where they reported very weak stellar wind value 0.004. For GRB 190114C wind is 2 times stronger compared to GRB 130427A, i.e. $\dot{M}_{-5}/v_8 = 0.02$, which is lower compared to stellar wind value reported by the MAGIC paper (MAGIC Collaboration et al. 2019b). In all three GRBs, we found that the internal $\gamma\gamma$ absorption in the blastwave

is not important for the model parameters we have used but the redshift-dependent absorption is included to very high energy photons. In principle, gamma-rays absorbed in the EBL can initiate a cascade and secondary contributions to the overall emission can be important if the intergalactic magnetic field is $\lesssim 10^{-19}$ G (see, e.g., Razzaque et al. 2004; Ando 2004; Murase et al. 2007). We do not, however, discuss this here. The MAGIC discovery paper on GRB 190114C have discussed the importance of KN effects and attenuations in the jet will shape the emission (MAGIC Collaboration et al. 2019b). Derishev & Piran (2019) found that Thomson scattering can be used in compared to the Klein-Nishina effect for this burst. We also found that the SSC emission in the Thomson regime can be used to model the sub-TeV observations of GRB 190114C. The Y parameter in equation (13) is of the order of one for all three GRBs we have modelled. We have used the analytical and smooth approximation for the estimation of SSC flux in this work. These two scenarios are compared in Figure 4 for GRB 190114C where grey solid lines represent the analytical approximation and the dotted orange curves represent the smooth approximation. Using the sub-TeV component we can find Thomson approximation useful for the multi-wavelength interpretation of GRB 190114C. In other two GRBs we study the emission in the Thomson approximation only in this work.

8 CONCLUSION

In conclusions, our synchrotron-SSC modelling proves to be useful in fitting multiwavelength afterglow data from long and short GRBs, including VHE data. Modelling these data sheds light on the GRB blastwave models and physical parameters involved in radio to VHE gamma-ray emission. The predicted SSC emission is less dominant in GRB 090510 and significant for GRB 130427A. The detection of this component in GRB 190114C is important to study the shock energy distributions in electrons and magnetic fields, and the environment surrounding the GRBs. The frequent detection of TeV component in GRB afterglows by upcoming CTA and the Large High Altitude Air Shower Observatory (LHASSO) (Cherenkov Telescope Array Consortium et al. 2019; Bai et al. 2019) will enrich GRB afterglow models.

9 ACKNOWLEDGEMENTS

We thank the anonymous referee for his insightful comments and suggestions. We are thankful to X.-Y. Wang and N. Fraija and S. B. Pandey for reading the manuscript and comments, R. J. Britto for providing the python script for the optical depth calculation, R. Liu, V. Chand for helpful discussions and M. Arimoto for his comments. The research work of J.C.J. was supported by a GES fellowship at the University of Johannesburg, where most part of the work is completed. S.R. acknowledges support from the National Research Foundation (South Africa) with Grant No. 111749 (CPRR).

DATA AVAILABILITY

The data used in this article are available in the article and in its online supplementary material. The code used for the SSC calculations can be shared on reasonable request to the corresponding author.

REFERENCES

- Abdalla H. et al., 2019, *Nature*, 575, 464
 Ackermann M. et al., 2014, *Science*, 343, 42
 Ajello M. et al., 2020, *ApJ*, 890, 9
 Ando S., 2004, *MNRAS*, 354, 414
 Bai X. et al., 2019, arXiv e-prints, arXiv:1905.02773
 Berger E., 2014, *ARA&A*, 52, 43
 Blandford R. D., McKee C. F., 1976, *Physics of Fluids*, 19, 1130
 Brown R. W., Mikaelian K. O., Gould R. J., 1973, *Astrophys. Lett.*, 14, 203
 Castro-Tirado A. J. et al., 2019, *GRB Coordinates Network*, 23708, 1
 Chand V. et al., 2020, arXiv e-prints, arXiv:2001.00648
 Cherenkov Telescope Array Consortium et al., 2019, *Science with the Cherenkov Telescope Array*
 Chevalier R. A., Li Z.-Y., 2000, *ApJ*, 536, 195
 Chiang J., Dermer C. D., 1999, *ApJ*, 512, 699
 Corsi A., Guetta D., Piro L., 2010, *ApJ*, 720, 1008
 Costa E. et al., 1997, *Nature*, 387, 783
 Dai Z. G., Lu T., 1998, *MNRAS*, 298, 87
 de Naurois M., 2019, *The Astronomer's Telegram*, 13052, 1
 De Pasquale M. et al., 2010, *ApJ*, 709, L146
 Derishev E., Piran T., 2019, *ApJ*, 880, L27
 Dermer C. D., Menon G., 2009, *High Energy Radiation from Black Holes: Gamma Rays, Cosmic Rays, and Neutrinos*, Princeton University Press
 Fan Y.-Z. et al., 2013, *ApJ*, 776, 95
 Finke J. D., Razzaque S., Dermer C. D., 2010, *ApJ*, 712, 238
 Fraija N., Barniol Duran R., Dichiarà S., Beniamini P., 2019a, *ApJ*, 883, 162
 Fraija N., Dichiarà S., Pedreira A. C. C. d. E. S., Galvan-Gamez A., Becerra R. L., Barniol Duran R., Zhang B. B., 2019b, *ApJ*, 879, L26
 Fraija N. et al., 2019c, *ApJ*, 885, 29
 Fraija N., Lee W., Veres P., 2016a, *ApJ*, 818, 190
 Fraija N., Lee W. H., Veres P., Barniol Duran R., 2016b, *ApJ*, 831, 22
 Funk S., Hinton J. A., CTA Consortium, 2013, *Astroparticle Physics*, 43, 348
 Gao H., Lei W.-H., Zou Y.-C., Wu X.-F., Zhang B., 2013, *New A Rev.*, 57, 141
 Gehrels N., Razzaque S., 2013, *Frontiers of Physics*, 8, 661
 Ghirlanda G., Ghisellini G., Nava L., 2010, *A&A*, 510, L7
 Ghisellini G., Ghirlanda G., Nava L., Celotti A., 2010, *MNRAS*, 403, 926
 Gould R. J., Schröder G. P., 1967, *Phys. Rev.*, 155, 1404
 Granot J., Nakar E., Piran T., 2003, *Nature*, 426, 138
 Granot J., Piran T., Sari R., 1999, *ApJ*, 527, 236
 Granot J., Sari R., 2002, *ApJ*, 568, 820
 He H.-N., Wu X.-F., Toma K., Wang X.-Y., Mészáros P., 2011, *ApJ*, 733, 22
 Kouveliotou C. et al., 2013, *ApJ*, 779, L1
 Kumar P., Barniol Duran R., 2009, *MNRAS*, 400, L75
 Kumar P., Zhang B., 2015, *Phys. Rep.*, 561, 1
 Laskar T. et al., 2019, *ApJ*, 878, L26
 Laskar T. et al., 2013a, *ApJ*, 776, 119
 Laskar T. et al., 2013b, *ApJ*, 776, 119
 Levan A. J., Cenko S. B., Perley D. A., Tanvir N. R., 2013, *GRB Coordinates Network*, 14455, 1
 Liu R.-Y., Wang X.-Y., Wu X.-F., 2013, *ApJ*, 773, L20
 MAGIC Collaboration et al., 2019a, *Nature*, 575, 455
 MAGIC Collaboration et al., 2019b, *Nature*, 575, 459
 Maselli A. et al., 2014, *Science*, 343, 48
 Melandri A. et al., 2014, *A&A*, 567, A29
 Meszaros P., Rees M. J., 1994, *MNRAS*, 269, L41
 Mészáros P., Rees M. J., 1997, *ApJ*, 476, 232
 Meszaros P., Rees M. J., Papathanassiou H., 1994, *ApJ*, 432, 181
 Murase K., Asano K., Nagataki S., 2007, *ApJ*, 671, 1886
 Paczynski B., Rhoads J. E., 1993, *ApJ*, 418, L5
 Panaitescu A., Kumar P., 2000, *ApJ*, 543, 66
 Panaitescu A., Kumar P., 2001, *ApJ*, 560, L49
 Panaitescu A., Mészáros P., 1998, *ApJ*, 493, L31

- Panaitescu A., Mészáros P., 1999, *ApJ*, 526, 707
- Panaitescu A., Vestrand W. T., Woźniak P., 2013, *MNRAS*, 436, 3106
- Pandey S. B. et al., 2010, *ApJ*, 714, 799
- Piran T., 1999, *Phys. Rep.*, 314, 575
- Rau A., McBreen S., Kruehler T., 2009, *GRB Coordinates Network*, 9353, 1
- Razzaque S., 2010, *ApJ*, 724, L109
- Razzaque S., 2013, *Phys. Rev. D*, 88, 103003
- Razzaque S., Dermer C. D., Finke J. D., 2009, *ApJ*, 697, 483
- Razzaque S., Dermer C. D., Finke J. D., 2010, *The Open Astronomy Journal*, 3, 150
- Razzaque S., Mészáros P., Zhang B., 2004, *ApJ*, 613, 1072
- Rees M. J., Meszaros P., 1992, *MNRAS*, 258, 41P
- Rees M. J., Mészáros P., 1998, *ApJ*, 496, L1
- Ronchi M. et al., 2020, *A&A*, 636, A55
- Rybicki G. B., Lightman A. P., 1986, *Radiative Processes in Astrophysics*, p. 400
- Sari R., 1997, *ApJ*, 489, L37
- Sari R., Esin A. A., 2001, *ApJ*, 548, 787
- Sari R., Piran T., 1999, *ApJ*, 520, 641
- Sari R., Piran T., Halpern J. P., 1999, *ApJ*, 519, L17
- Sari R., Piran T., Narayan R., 1998, *ApJ*, 497, L17
- Tam P.-H. T., Tang Q.-W., Hou S.-J., Liu R.-Y., Wang X.-Y., 2013, *ApJ*, 771, L13
- Thomas J. K., Moharana R., Razzaque S., 2017, *Phys. Rev. D*, 96, 103004
- van Paradijs J. et al., 1997, *Nature*, 386, 686
- Vestrand W. T. et al., 2014, *Science*, 343, 38
- Vietri M., 1997, *ApJ*, 478, L9
- Wang X.-Y., Liu R.-Y., Zhang H.-M., Xi S.-Q., Zhang B., 2019, *arXiv e-prints*, arXiv:1905.11312
- Zhang B., 2019, *Nature*, 575, 448
- Zhang B., Mészáros P., 2001, *ApJ*, 559, 110
- Zhang B., Mészáros P., 2004a, *International Journal of Modern Physics A*, 19, 2385
- Zhang B., Mészáros P., 2004b, *International Journal of Modern Physics A*, 19, 2385
- Zhang H., Christie I., Petropoulou M., Rueda-Becerril J. M., Giannios D., 2019, *arXiv e-prints*, arXiv:1910.14049

APPENDIX A**Synchrotron self-absorption frequency**

The synchrotron spectra in equations (16) and (17) have the lowest frequency break at ν_a , below which the synchrotron spectrum becomes harder by an index $2/3$ due to synchrotron-self-absorption (Rybicki & Lightman 1986). We describe here the derivation of self-absorption frequency ν_a for the blastwave in the circumburst medium. To calculate this we first define the self-absorption coefficient based on (Granot et al. 1999),

$$\alpha'_{\nu'} = \frac{p+2}{8\pi m_e \nu'^2} \int_{\gamma_{\text{in}}}^{\infty} P'(\gamma'_e) \frac{N_e(\gamma_e)}{\gamma_e} d\gamma_e. \quad (\text{A-1})$$

Here the electron distribution $N_e(\gamma_e)$ is independent of the fast- and slow-cooling. From the unmodified electron distribution, defined previously we have

$$N_e(\gamma_e) = n'(p-1)\gamma_m'^{p-1} \gamma_e^{-p}, \quad (\text{A-2})$$

where n' is the density of the electrons in the jet frame and is related to the ambient density $n(R)$, with $n' \approx 4\Gamma_g n(R)$ (Blandford & McKee 1976; Granot et al. 1999) For the electron Lorentz factor γ_e we can calculate the emitted frequency ν'_{sy} and emitted power $P'(\gamma'_e)$ as (Granot et al. 1999)

$$\nu'_{sy} = \frac{3q_e B'(t) \gamma_e'^2 \sin \alpha}{4\pi m_e c} \quad (\text{A-3})$$

and

$$P'(\gamma'_e) = \frac{2^{5/3} \pi q_e^3 B'(t) \sin \alpha}{\Gamma(\frac{1}{3}) m_e c^2} \left(\frac{\nu'}{\nu'_{sy}} \right)^{1/3}, \quad (\text{A-4})$$

respectively. Here, Γ represents the Gamma function. Using equations (A-1-A-4) we can derive the expression for the self-absorption coefficient as

$$\alpha'_{\nu'} = \frac{(p+2)(p-1)n'}{8\pi m_e \nu'^{5/3}} \frac{2^{5/3} \pi q_e^3 B'(t) \sin \alpha}{\Gamma(\frac{1}{3}) m_e c^2} \times \left[\frac{4\pi m_e c}{3q_e B'(t) \sin \alpha} \right]^{1/3} \gamma_m'^{p-1} \int_{\gamma_m'}^{\infty} \gamma_e^{-(p+5/3)} d\gamma_e. \quad (\text{A-5})$$

We have further simplified this expression using an average value of $\sin^{3/2} \alpha$, which is equal to $(\sqrt{\pi}/5)\Gamma(1/3)\Gamma(5/6)$, as

$$\alpha'_{\nu'} = 4.7 \times 10^{-10} \left[\frac{(p+2)(p-1)}{(3p+2)\nu'^{5/3}} \right] q_e^{8/3} m_e^{-5/3} \times m_p^{1/3} \epsilon_B^{1/3} \Gamma_g(t)^{5/3} n(R)^{4/3} \gamma_m'^{-5/3}. \quad (\text{A-6})$$

We derive the absorption coefficients in the ISM and wind cases as

$$\alpha'_{\nu'}(\text{ISM}) = 925.6 \frac{(p+2)(p-1)}{(3p+2)\nu'^{5/3}} \epsilon_B^{1/3} n_0^{4/3} \gamma_m'^{-5/3} \Gamma_g(t)^{5/3} \quad (\text{A-7})$$

and

$$\alpha'_{\nu'}(\text{Wind}) = 2 \times 10^{50} \frac{(p+2)(p-1)}{(3p+2)\nu'^{5/3}} \times \epsilon_B^{1/3} A_*^{4/3} R(t)^{-8/3} \gamma_m'^{-5/3} \Gamma_g(t)^{5/3}, \quad (\text{A-8})$$

respectively.

From the above expressions of $\alpha'_{\nu'}$, at the absorption frequency $\nu' = \nu'_a$, the condition that must be satisfied is $\alpha'_{\nu'_a} R(t)/\Gamma_g(t) = 1$. Further, following Dermer & Menon (2009) for the slow-cooling case $\gamma'_e = \gamma'_m$ and for the fast-cooling case $\gamma'_e = \gamma'_c$ provides the general expression for the synchrotron-self-absorption frequency as

$$\nu'_{a[s,f]}(\text{ISM}) = 4253 \frac{(p+2)(p-1)}{(3p+2)} \times \left[\epsilon_B^{1/3} n_0^{4/3} \gamma_{[m,c]}'^{-5/3} \Gamma_g(t)^{8/3} \frac{ct}{1+z} \right]^{3/5} \quad (\text{A-9})$$

and

$$\nu'_{a[s,f]}(\text{Wind}) = 8.3 \times 10^{48} \frac{(p+2)(p-1)}{(3p+2)} \times \left[\epsilon_B^{1/3} A_*^{4/3} \gamma_{[m,c]}'^{-5/3} \Gamma_g(t)^{-8/3} \left(\frac{ct}{1+z} \right)^{-5/3} \right]^{3/5}, \quad (\text{A-10})$$

respectively, for the ISM and wind medium. The subscripts $[s, f] \rightarrow [m, c]$ refer to the slow- and fast-cooling cases. The self-absorption frequency depends on the spectral index p of the electrons for both the fast- and slow-cooling scenarios, due to their dependence on the minimum Lorentz factor γ'_m . We report numerical values of ν_a in the Appendix for different blastwave evolution scenarios.

APPENDIX B

Below we give numerical expressions for the blastwave evolution parameters, synchrotron parameters and break frequencies, and SSC parameters and break frequencies. These values are described for the adiabatic blastwaves when they propagate in the constant density medium (ISM) or in a wind-type environment. Here $d_{28} = d_L/10^{28}$ cm and $t_2 = t/100$ s and $\nu_{eV} = \nu/1\text{eV}$.

Adiabatic blastwave in the constant density medium

$$\Gamma_g = 155 (1+z)^{3/8} n_0^{-1/8} E_{55}^{1/8} t_2^{-3/8} \quad (\text{B-1})$$

$$R = 1.2 \times 10^{18} (1+z)^{-1/4} n_0^{-1/4} E_{55}^{1/4} t_2^{1/4} \text{ cm} \quad (\text{B-2})$$

$$B' = 19.0 (1+z)^{3/8} \epsilon_{B,-1}^{1/2} n_0^{3/8} E_{55}^{1/8} t_2^{-3/8} \text{ G} \quad (\text{B-3})$$

Table 2. The closure relations between the temporal index α and spectral index β in various afterglow models for synchrotron and inverse Compton emission with flux distribution $F_\nu \propto t^\alpha \nu^\beta$.

	β	α	$\alpha(\beta)$
Synchrotron emission			
Adiabatic (ISM) slow cooling			
$\nu < \nu_{a, sy}$	2	1/2	$\beta/4$
$\nu_{a, sy} \leq \nu \leq \nu_{m, sy}$	1/3	1/2	$3\beta/2$
$\nu_{m, sy} < \nu < \nu_{c, sy}$	$-(p-1)/2$	$-3(p-1)/4$	$3\beta/2$
$\nu \geq \nu_{c, sy}$	$-p/2$	$-(3p-2)/4$	$(3\beta+1)/2$
Adiabatic (ISM) fast cooling			
$\nu < \nu_{a, sy}$	2	1	$\beta/2$
$\nu_{a, sy} \leq \nu \leq \nu_{c, sy}$	1/3	1/6	$\beta/2$
$\nu_{c, sy} < \nu < \nu_{m, sy}$	$-1/2$	$-1/4$	$\beta/2$
$\nu \geq \nu_{m, sy}$	$-p/2$	$-(3p-2)/4$	$(3\beta+1)/2$
Adiabatic (wind) slow cooling			
$\nu < \nu_{a, sy}$	2	1	$\beta/2$
$\nu_{a, sy} \leq \nu \leq \nu_{m, sy}$	1/3	0	$(3\beta-1)/2$
$\nu_{m, sy} < \nu < \nu_{c, sy}$	$-(p-1)/2$	$-(3p-1)/4$	$(3\beta-1)/2$
$\nu \geq \nu_{c, sy}$	$-p/2$	$-(3p-2)/4$	$(3\beta+1)/2$
Adiabatic (wind) fast cooling			
$\nu < \nu_{a, sy}$	2	2	β
$\nu_{a, sy} \leq \nu \leq \nu_{c, sy}$	1/3	$-2/3$	$-(\beta+1)/2$
$\nu_{c, sy} < \nu < \nu_{m, sy}$	$-1/2$	$-1/4$	$-(\beta+1)/2$
$\nu \geq \nu_{m, sy}$	$-p/2$	$-(3p-2)/4$	$(3\beta+1)/2$
SSC emission			
Adiabatic(ISM) slow cooling			
$\nu < \nu_{a, ssc}$	2	9/4	$9\beta/8$
$\nu_{a, ssc} \leq \nu \leq \nu_{m, ssc}$	1/3	1	3β
$\nu_{m, ssc} < \nu < \nu_{c, ssc}$	$-(p-1)/2$	$-(9p-11)/8$	$(9\beta+1)/4$
$\nu \geq \nu_{c, ssc}$	$-p/2$	$-(9p-10)/8$	$(9\beta+5)/4$
Adiabatic(ISM) fast cooling			
$\nu < \nu_{a, ssc}$	2	3/4	$3\beta/8$
$\nu_{a, ssc} \leq \nu \leq \nu_{c, ssc}$	1/3	1/3	β
$\nu_{c, ssc} < \nu < \nu_{m, ssc}$	$-1/2$	1/8	$-\beta/4$
$\nu \geq \nu_{m, ssc}$	$-p/2$	$-(9p-10)/8$	$(9\beta+5)/4$
Adiabatic (wind) slow cooling			
$\nu < \nu_{a, ssc}$	2	3/2	$3\beta/4$
$\nu_{a, ssc} \leq \nu \leq \nu_{m, ssc}$	1/3	$-1/3$	$-\beta$
$\nu_{m, ssc} < \nu < \nu_{c, ssc}$	$-(p-1)/2$	$-p$	$2\beta-1$
$\nu \geq \nu_{c, ssc}$	$-p/2$	$-p+1$	$2\beta+1$
Adiabatic (wind) fast cooling			
$\nu < \nu_{a, ssc}$	2	11/6	$11\beta/12$
$\nu_{a, ssc} \leq \nu \leq \nu_{c, ssc}$	1/3	$-5/3$	-5β
$\nu_{c, ssc} < \nu < \nu_{m, ssc}$	$-1/2$	0	$\beta+1/2$
$\nu \geq \nu_{m, ssc}$	$-p/2$	$-p+1$	$2\beta+1$

$$\gamma'_m = 2.8 \times 10^4 \left(\frac{p-2}{p-1} \right) (1+z)^{3/8} \epsilon_{e,-1} n_0^{-1/8} E_{55}^{1/8} t_2^{-3/8} \quad (\text{B-4})$$

$$\gamma'_c = 137.8 (1+z)^{-1/8} \epsilon_{B,-1}^{-1} n_0^{-5/8} E_{55}^{-3/8} t_2^{1/8} (1+Y)^{-1} \quad (\text{B-5})$$

$$\gamma'_s = 8.5 \times 10^6 (1+z)^{-3/16} \epsilon_{B,-1}^{-1/4} n_0^{-3/16} \phi_1^{-1/2} E_{55}^{-1/16} t_2^{3/16} (1+Y)^{-1/2} \quad (\text{B-6})$$

$$h\nu_{\alpha,\text{fast}} = 9.0 \times 10^{-2} \left[\frac{(p+2)(p-1)}{(3p+2)} \right]^{3/5} (1+z)^{-1/2} \epsilon_{B,-1}^{6/5} n_0^{11/10} E_{55}^{7/10} t_2^{-1/2} (1+Y) \text{ eV} \quad (\text{B-7})$$

$$h\nu_{\alpha,\text{slow}} = 4.4 \times 10^{-4} \frac{(p+2)^{3/5} (p-1)^{8/5}}{(3p+2)^{3/5} (p-2)} (1+z)^{-1} \epsilon_{B,-1}^{1/5} \epsilon_{e,-1}^{-1} n_0^{3/5} E_{55}^{1/5} \text{ eV} \quad (\text{B-8})$$

$$h\nu_c = 1.0 (1+z)^{-1/2} \epsilon_{B,-1}^{-3/2} n_0^{-1} E_{55}^{-1/2} t_2^{-1/2} (1+Y)^{-2} \text{ eV} \quad (\text{B-9})$$

$$h\nu_m = 41.3 \left(\frac{p-2}{p-1} \right)^2 (1+z)^{1/2} \epsilon_{B,-1}^{1/2} \epsilon_{e,-1}^2 E_{55}^{1/2} t_2^{-3/2} \text{ keV} \quad (\text{B-10})$$

$$h\nu_s = 3.7 (1+z)^{-5/8} \phi_1^{-1} n_0^{-1/8} E_{55}^{1/8} t_2^{-3/8} (1+Y)^{-1} \text{ GeV} \quad (\text{B-11})$$

The above set of frequencies builds-up the spectral energy distribution for synchrotron emission. For these set of frequencies we also calculate the time when they will appear in the spectrum. We list two most frequent time breaks, t_c and t_m ,

$$t_c = 94.1 (1+z)^{-1} \epsilon_{B,-1}^{-3} n_0^{-2} E_{55}^{-1} (1+Y)^{-4} \nu_{c,\text{eV}}^{-2} \text{ s} \quad (\text{B-12})$$

$$t_m = 1.2 \times 10^5 \left(\frac{p-2}{p-1} \right)^{4/3} (1+z)^{1/3} \epsilon_{B,-1}^{1/3} \epsilon_{e,-1}^{4/3} E_{55}^{1/3} \nu_{m,\text{eV}}^{-2/3} \text{ s} \quad (\text{B-13})$$

The synchrotron transition time for the fast to slow cooling is calculated for the time when ν_m and ν_c coincides, i.e. $\nu_m(t_0) = \nu_c(t_0)$, The synchrotron and effective inverse-Compton cooling times are given by,

$$t_0 = 4.3 \times 10^6 \left(\frac{p-2}{p-1} \right)^2 (1+z) \epsilon_{B,-1}^2 \epsilon_{e,-1}^2 n_0 E_{55} \text{ s} \quad (\text{B-14})$$

$$t_0^{\text{ssc}} = 4.3 \times 10^6 \left(\frac{p-2}{p-1} \right)^2 (1+z) \epsilon_{B,-1}^2 \epsilon_{e,-1}^2 n_0 E_{55} (1+Y)^2 \text{ s} \quad (\text{B-15})$$

Now we have listed the set of break frequencies for the SSC component. The SSC break frequencies are,

$$h\nu_{\alpha,\text{ssc,fast}} = 3.5 \left[\frac{(p+2)(p-1)}{3p+2} \right]^{3/5} (1+z)^{-3/4} \epsilon_{B,-1}^{-4/5} n_0^{-3/20} E_{55}^{-1/20} t_2^{-1/4} (1+Y)^{-1} \text{ keV} \quad (\text{B-16})$$

$$h\nu_{\alpha,\text{ssc,slow}} = 0.7 \left[\frac{(p+2)^{3/5} (p-1)^{-2/5} (p-2)}{(3p+2)^{3/5}} \right] (1+z)^{-1/4} \epsilon_{B,-1}^{1/5} \epsilon_{e,-1}^{7/20} E_{55}^{9/20} t_2^{-3/4} \text{ MeV} \quad (\text{B-17})$$

$$h\nu_{c,\text{ssc}} = 0.04 (1+z)^{-3/4} \epsilon_{B,-1}^{-7/2} n_0^{-9/4} E_{55}^{-5/4} t_2^{-1/4} (1+Y)^{-4} \text{ MeV} \quad (\text{B-18})$$

$$h\nu_{m,\text{ssc}} = 66.5 \left(\frac{p-2}{p-1} \right)^4 (1+z)^{5/4} \epsilon_{B,-1}^{1/2} \epsilon_{e,-1}^4 n_0^{-1/4} E_{55}^{3/4} t_2^{-9/4} \text{ TeV} \quad (\text{B-19})$$

The break times for minimum and cooling frequencies are defined as,

$$t_{c,\text{ssc}} = 2.6 \times 10^{20} (1+z)^{-3} \epsilon_{B,-1}^{-14} n_0^{-9} E_{55}^{-5} (1+Y)^{-16} \nu_{c,\text{ssc,eV}}^{-4} \text{ s} \quad (\text{B-20})$$

$$t_{m,\text{ssc}} = 1.4 \times 10^8 \left(\frac{p-2}{p-1} \right)^{16/9} (1+z)^{5/9} \epsilon_{B,-1}^{2/9} \epsilon_{e,-1}^{16/9} n_0^{-1/9} E_{55}^{1/3} \nu_{m,\text{ssc,eV}}^{-4/9} \text{ s} \quad (\text{B-21})$$

The maximum flux values for the synchrotron and SSC emission are,

$$f_{\nu,\text{max}} = 377.1 (1+z)^{-1} \epsilon_{B,-1}^{1/2} n_0^{1/2} E_{55} d_{28}^{-2} \text{ Jy}. \quad (\text{B-22})$$

$$f_{\nu,\text{max,ssc}} = 7.7 \times 10^{-4} (1+z)^{-5/4} \epsilon_{B,-1}^{1/2} n_0^{5/4} E_{55}^{5/4} t_2^{1/4} d_{28}^{-2} \text{ Jy}. \quad (\text{B-23})$$

Adiabatic blastwave into the wind medium

The parameters have the same physical meaning as for the expressions defined above.

$$\Gamma_g = 113.6 (1+z)^{1/4} A_\star^{-1/4} E_{55}^{1/4} t_2^{-1/4}. \quad (\text{B-24})$$

$$R = 3.1 \times 10^{17} (1+z)^{-1/2} A_\star^{-1/2} E_{55}^{1/2} t_2^{1/2} \text{ cm}. \quad (\text{B-25})$$

$$B' = 24.8 (1+z)^{3/4} \epsilon_{B,-1}^{1/2} A_\star^{3/4} E_{55}^{-1/4} t_2^{-3/4} \text{ G}. \quad (\text{B-26})$$

$$\gamma'_m = 2.1 \times 10^4 \left(\frac{p-2}{p-1} \right) (1+z)^{1/4} \epsilon_{e,-1} A_\star^{-1/4} E_{55}^{1/4} t_2^{-1/4} \quad (\text{B-27})$$

$$\gamma'_c = 111.0 (1+z)^{-3/4} \epsilon_{B,-1}^{-1} A_\star^{-5/4} E_{55}^{1/4} t_2^{3/4} (1+Y)^{-1} \quad (\text{B-28})$$

$$\gamma'_s = 7.4 \times 10^6 (1+z)^{-3/8} \epsilon_{B,-1}^{-1/4} \phi_1^{-1/2} A_\star^{-3/8} E_{55}^{1/8} t_2^{3/8} (1+Y)^{-1/2} \quad (\text{B-29})$$

$$h\nu_{a,\text{fast}} = 4.3 \times 10^{-2} \left[\frac{(p-1)(p+2)}{(3p+2)} \right]^{3/5} (1+z)^{3/5} \epsilon_{B,-1}^{6/5} A_\star^{11/5} E_{55}^{-2/5} t_2^{-8/5} (1+Y) \text{ eV}. \quad (\text{B-30})$$

$$h\nu_{a,\text{slow}} = 2.3 \times 10^{-4} \frac{(p-1)^{8/5} (p+2)^{3/5}}{(3p+2)^{3/5} (p-2)} (1+z)^{-2/5} \epsilon_{B,-1}^{1/5} \epsilon_{e,-1}^{-1} A_\star^{6/5} E_{55}^{-2/5} t_2^{-3/5} \text{ eV}. \quad (\text{B-31})$$

$$h\nu_c = 0.6 (1+z)^{-3/2} \epsilon_{B,-1}^{-3/2} A_\star^{-2} E_{55}^{1/2} t_2^{1/2} (1+Y)^{-2} \text{ eV}. \quad (\text{B-32})$$

$$h\nu_m = 2.1 \times 10^4 \left(\frac{p-2}{p-1} \right)^2 (1+z)^{1/2} \epsilon_{B,-1}^{1/2} \epsilon_{e,-1}^2 E_{55}^{1/2} t_2^{-3/2} \text{ eV}. \quad (\text{B-33})$$

$$h\nu_s = 2.7 (1+z)^{-3/4} \phi_1^{-1} A_\star^{-1/4} E_{55}^{1/4} t_2^{-1/4} (1+Y)^{-1} \text{ GeV}. \quad (\text{B-34})$$

$$t_c = 1.6 \times 10^2 (1+z)^3 \epsilon_{B,-1}^3 A_\star^4 E_{55}^{-1} (1+Y)^4 \nu_{c,\text{eV}}^2 \text{ s} \quad (\text{B-35})$$

$$t_m = 7.6 \times 10^4 \left(\frac{p-2}{p-1} \right)^{4/3} (1+z)^{1/3} \epsilon_{B,-1}^{1/3} \epsilon_{e,-1}^{4/3} E_{55}^{1/3} \nu_{m,\text{eV}}^{-2/3} \text{ s} \quad (\text{B-36})$$

$$t_0 = 2.0 \times 10^4 \left(\frac{p-2}{p-1} \right) (1+z) \epsilon_{B,-1} \epsilon_{e,-1} A_\star \text{ s} \quad (\text{B-37})$$

$$t_0^{\text{ssc}} = 2.0 \times 10^4 \left(\frac{p-2}{p-1} \right) (1+z) \epsilon_{B,-1} \epsilon_{e,-1} A_\star (1+Y) \text{ s} \quad (\text{B-38})$$

$$h\nu_{a,\text{ssc,fast}} = 1.1 \left[\frac{(p+2)(p-1)}{3p+2} \right]^{3/5} (1+z)^{9/10} \epsilon_{B,-1}^{-4/5} A_\star^{-3/10} E_{55}^{1/10} t_2^{-1/10} (1+Y)^{-1} \text{ keV}. \quad (\text{B-39})$$

$$h\nu_{a,\text{ssc,slow}} = 0.2 \frac{(p-2)(p+2)^{3/5}}{(3p+2)^{3/5} (p-1)^{2/5}} (1+z)^{1/10} \epsilon_{B,-1}^{1/5} \epsilon_{e,-1} A_\star^{7/10} E_{55}^{1/10} t_2^{-11/10} \text{ MeV}. \quad (\text{B-40})$$

$$h\nu_{c,\text{ssc}} = 15.0 (1+z)^{-3} \epsilon_{B,-1}^{-7/2} A_\star^{-9/2} E_{55}^2 t_2^2 (1+Y)^{-4} \text{ keV}. \quad (\text{B-41})$$

$$h\nu_{m,\text{ssc}} = 19.0 \left(\frac{p-2}{p-1} \right)^4 (1+z) \epsilon_{B,-1}^{1/2} \epsilon_{e,-1}^4 E_{55} A_\star^{-1/2} t_2^{-2} \text{ TeV}. \quad (\text{B-42})$$

$$t_{c,\text{ssc}} = 0.8 (1+z)^{3/2} \epsilon_{B,-1}^{7/4} A_\star^{9/4} E_{55}^{-1/2} (1+Y)^2 \nu_{c,\text{ssc,eV}}^{1/2} \text{ s}. \quad (\text{B-43})$$

$$t_{m,\text{ssc}} = 4.3 \times 10^8 \left(\frac{p-2}{p-1} \right)^2 (1+z)^{1/2} \epsilon_{B,-1}^{1/4} \epsilon_{e,-1}^2 E_{55}^{1/2} \nu_{m,\text{ssc,eV}}^{-1/2} \text{ s} \quad (\text{B-44})$$

$$f_{\nu, \max} = 22.0 (1+z)^{-1/2} \epsilon_{B,-1}^{1/2} A_{\star} E_{55}^{1/2} t_2^{-1/2} d_{28}^{-2} \text{ Jy.} \quad (\text{B-45})$$

$$f_{\nu, \max, \text{SSC}} = 3.8 \times 10^{-5} \epsilon_{B,-1}^{1/2} A_{\star}^{5/2} t_2^{-1} d_{28}^{-2} \text{ Jy.} \quad (\text{B-46})$$

This figure "sed_grb_190114C.png" is available in "png" format from:

<http://arxiv.org/ps/1911.01558v3>